Catalysis Science & **Technology**



PAPER

View Article Online



Cite this: Catal. Sci. Technol., 2023, **13**, 6999

single-atom Fe-catalysts† Sungil Hong, (Da Minttu M. Kauppinen, (Db Evan V. Miu, (Da

methane oxidation over graphene-stabilized

First-principles microkinetic modeling of partial

Giannis Mpourmpakis (10 ** and Henrik Grönbeck**)

Catalytic conversion of CH₄ to transportable liquid hydrocarbons via partial oxidation is a promising avenue towards efficient utilization of natural gas. Single Fe atoms on N-functionalized graphene (Fe N_4 /GN) have recently been shown to be active for partial CH₄ oxidation with H₂O₂ at room temperature. Here, density functional theory (DFT) calculations combined with mean-field microkinetic modeling (MKM) have been applied to obtain kinetic understanding of partial CH₄ oxidation with H₂O₂ to CH₃OH and CH₃OOH over FeN₄/GN. CH₃OH and CH₃OOH are found to be minor and major reaction products, respectively, with a selectivity in agreement with reported experimental data. The kinetic modeling reveals two pathways for CH₃OH production together with a dominant catalytic cycle for CH₃OOH formation. The selectivity is found to be sensitive to the temperature and H₂O₂ concentration, with the CH₃OH selectivity increasing with increasing temperature and decreasing H₂O₂ concentration. Turnover frequencies of both CH₃OH and CH₃OOH are found to decrease over time, due to a change in the Fe formal oxidation state from +6 to +4; Fe(+6) is more active, but less stable than Fe(+4). The present work unravels the detailed reaction mechanism for partial oxidation of methane by FeN₄/GN, rationalizes experimental observations and provides quidance for efficient room-temperature methane conversion by single-atom Fe-catalysts.

Received 25th September 2023. Accepted 9th November 2023

DOI: 10.1039/d3cy01335a

rsc.li/catalysis

Introduction

Natural gas is still one of the most important energy sources.¹ The share of natural gas in global energy production has gradually increased over the last decade due to its vast reserves and less CO2 released per produced energy unit compared to other fossil fuels.^{1,2} Nevertheless, natural gas associated with petroleum extraction has been flared since its utilization is not profitable and CH4 (the largest component of natural gas) has a much higher global warming potential than CO₂. The amount of natural gas flared worldwide is as much as 17% of the total natural gas consumption in the United States.^{1,4} CH₄ is flared because of challenges handling gaseous products at the sites of petroleum extraction and the lack of processes for small scale on-site catalytic conversion liquid products. The commercial CH₄-to-CH₃OH conversion process is presently syngas production followed by

Small-scale on-site catalytic conversion of CH₄ to liquid hydrocarbon could be a promising avenue toward valorizing natural gas that presently is being wasted. The liquid derivatives of CH4 can replace natural gas as a primary energy source since the storage and transportation of liquid products are safer and less costly than those of gaseous products. Further, the possible products, e.g., alcohols and olefins, are value-added chemicals with high industrial demand. Especially, methanol (CH3OH) is a valuable target chemical, since it can be used as both a fuel for combustion engines⁸ or fuel cells, ^{9,10} and chemical feedstock for a range of chemicals, such as methyl tertiary-butyl ether, 11 dimethyl ether,12 and formaldehyde.13 Hence, significant research has been recently devoted to study catalysts for direct partial CH₄ oxidation at low temperatures. Direct partial oxidation of CH₄ is challenging due to the chemical inertness of CH4. 14 High temperatures facilitate C-H bond activation, but with the risk of over-oxidation of CH₃OH to CO₂, as the C-H bond of CH₃-OH is weaker than that of CH₄.^{14,15} Thus, CH₄-to-CH₃OH conversion should be performed at low temperatures. Overoxidation could be suppressed by having well-defined catalytic sites with single metal centers embedded in an inert matrix. However, single metal centers may not be

Fischer-Tropsch synthesis, which are highly centralized and energy intensive processes.5-7

^a Department of Chemical & Petroleum Engineering, University of Pittsburgh, Pittsburgh, Pennsylvania 15261, USA. E-mail: gmpourmp@pitt.edu

^b Department of Physics and Competence Centre for Catalysis, Chalmers University of Technology, SE-412 96 Göteborg, Sweden. E-mail: ghj@chalmers.se

[†] Electronic supplementary information (ESI) available. See DOI: https://doi.org/ 10.1039/d3cy01335a

Metal- and metal oxide-based homogeneous catalysis for CH₄ activation has been widely studied since the 1980s. 17-23 Among many catalysts, CoO+ and FeO+ showed activity toward CH₄-to-CH₃OH conversion. 18,19 Periana and coworkers demonstrated high activity of Hg(II) and Pt(II) salts in a concentrated H₂SO₄ solution. ^{24,25} Moreover, partial oxidation of CH₄ can be performed over methane monooxygenases (MMOs) at room-temperature. 26-29 Despite the partial successes, homogeneous catalysis has intrinsic constraints for commercialization as it requires additional product separation processes, which has motivated research efforts in developing heterogeneous catalysts for CH₄ conversion. Especially, biomimetic partial oxidation of CH₄ using Fe- and Cu-based zeolite catalysts has attracted interest. The Fe sites of Fe-ZSM-5 obtain active oxygen species (α-oxygen) from nitrous oxide (N2O), which can convert CH4 to CH3OH.30-32 The active bi-nuclear Fe center of Fe-ZSM-5 resembles the diiron center of soluble-MMO enzymes. 30-32 Likewise, Cu-ZSM-5 catalysts have shown activity towards CH₄-to-CH₃OH conversion, mimicking particulate-MMO enzymatic systems, although the nature of the active centers has not been completely understood.33-35 One severe drawback of the zeolite-based catalysts is that they require elevated temperatures (≥200 °C) for the extraction of CH₃OH due to the hydrophilic nature of the zeolite framework. 33,36

In 2018, Cui and coworkers reported room-temperature activity for partial CH4 oxidation over N-functionalized single Fe atom catalyst stabilized on graphene (FeN₄/GN) with H₂O₂ as oxidant.37 The measured reaction products included CH3-OH, CH₃OOH, HOCH₂OOH, and HCOOH, where the two last species were suggested to originate from CH₃OH oxidation.³⁷ Over-oxidation of the reaction product to CO2 was significantly suppressed probably owing to the low operating temperature (25 °C) and the isolated nature of the active center (6.3% selectivity for CO₂).³⁷ The CH₄ conversion is comparable to, or higher than, that of zeolite-based catalysts operated at higher temperatures. 38,39

We have previously performed density functional theory (DFT) calculations to elucidate the reaction paths for partial oxidation over FeN₄/GN.⁴⁰ Plausible mechanisms were identified that demonstrated the role of H₂O₂ as a key reacting species to produce CH₃OH. 40 Moreover, the energetic span model proposed by Kozuch and Shaik⁴¹ was applied to estimate the turnover frequencies (TOFs) of different reaction pathways and get activity trends from individual reaction mechanisms. However, the energetic span model is an over-simplification in this case as it does not account for nested reaction paths and, moreover, does not properly account for the operating conditions, e.g., the reactant concentrations. In addition, our previous work focused primarily on mechanisms producing CH3OH without considering other products.⁴⁰

Herein, we develop a first-principles-based mean-field microkinetic model (MKM) for CH₄ conversion on FeN₄/GN catalyst. First-principles-based MKM is a powerful tool to provide unbiased kinetic information on TOF, selectivity, apparent activation energy, reaction-orders, surface coverages and rate-controlling reaction steps over a variety of complicated heterogeneous catalytic systems. 42-49 The multiple reaction mechanisms determined using the DFT calculations are coupled in the MKM to examine the kinetic properties of nested catalytic cycles with a dynamic change in the Fe oxidation state.40 Moreover, to compare with experiments, additional reaction mechanisms for the conversion of CH₄ to methyl hydroperoxide (CH₃OOH), which is another major reaction product,³⁷ have been investigated with DFT and included in the kinetic modeling. The present first-principles-based MKM rationalizes observations, demonstrating the capability of MKM to model a highly complex reaction network and provide a fundamental understanding of the active nature of FeN4/GN catalyst. This work can guide further efforts on designing efficient catalysts for CH4 conversion to value-added fuels and chemicals.

Computational details

Density functional theory calculations

Density functional theory (DFT) calculations were performed with the Gaussian 09 software package at the B3LYP/6-31G(d) level of theory.⁵⁰⁻⁵² Comparative computations with the M06-2X functional yields similar results. 40 Vibrational frequency calculations were performed to confirm that the stationary points are either minima or saddle points. The optimized transition state (TS) structures were confirmed to connect the corresponding reactants and products by intrinsic reaction coordinate calculations.53 FeN4/GN is modeled having a central single Fe atom, which is anchored by 4 N atoms to a graphene flake (represented by 26 C atoms terminated by H atoms on the edges). The reaction energetics depend weakly on the size of the graphene flake (Fig. S1†). Two different types of active centers were considered:40 singly oxygenated (mono-oxo) and doubly oxygenated (di-oxo) centers (Fig. 1). As the reaction takes place in water experimentally,³⁷ solvent effects were considered in all calculations by applying the conductor-like polarizable continuum model (CPCM)⁵⁴ with water as the solvent. The reaction energetics were described in terms of Gibbs free energy at 298.15 K and 1 atm, unless otherwise specified in the results. The enthalpic and entropic contributions to Gibbs free energy of reaction are assumed to be constant within the small temperature range considered

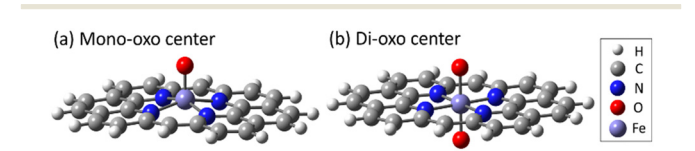


Fig. 1 Catalyst structures with (a) mono-oxo and (b) di-oxo FeN₄/GN centers.

(278.15-318.15 K). Hence, Gibbs free energy of reaction at temperature T was calculated as:

$$\Delta G_{\text{rxn},T} = \Delta H_{\text{rxn},298,15 \text{ K}} - T \times \Delta S_{\text{rxn},298,15 \text{ K}}$$
 (1)

Entropy values reported in ref. 55 (at 298.15 K in water) were used for all the molecules except CH3OOH, which is unavailable in the literature. The entropy of CH₃OOH was therefore determined by multiplying a factor of 0.62 to the gas-phase DFT-determined entropy, based on the simple scaling relation reported in ref. 56. This scaling factor is similar to how the experimental and gas-phase calculated entropies of H₂O₂ scale (Table S1†), demonstrating the validity of this selection considering the structural similarity between the CH₃OOH and H₂O₂ molecules. For the structures involving the catalyst surfaces, real vibrational frequencies lower than 100 cm⁻¹ were replaced by 100 cm⁻¹ when determining entropies and free energies to reduce errors that

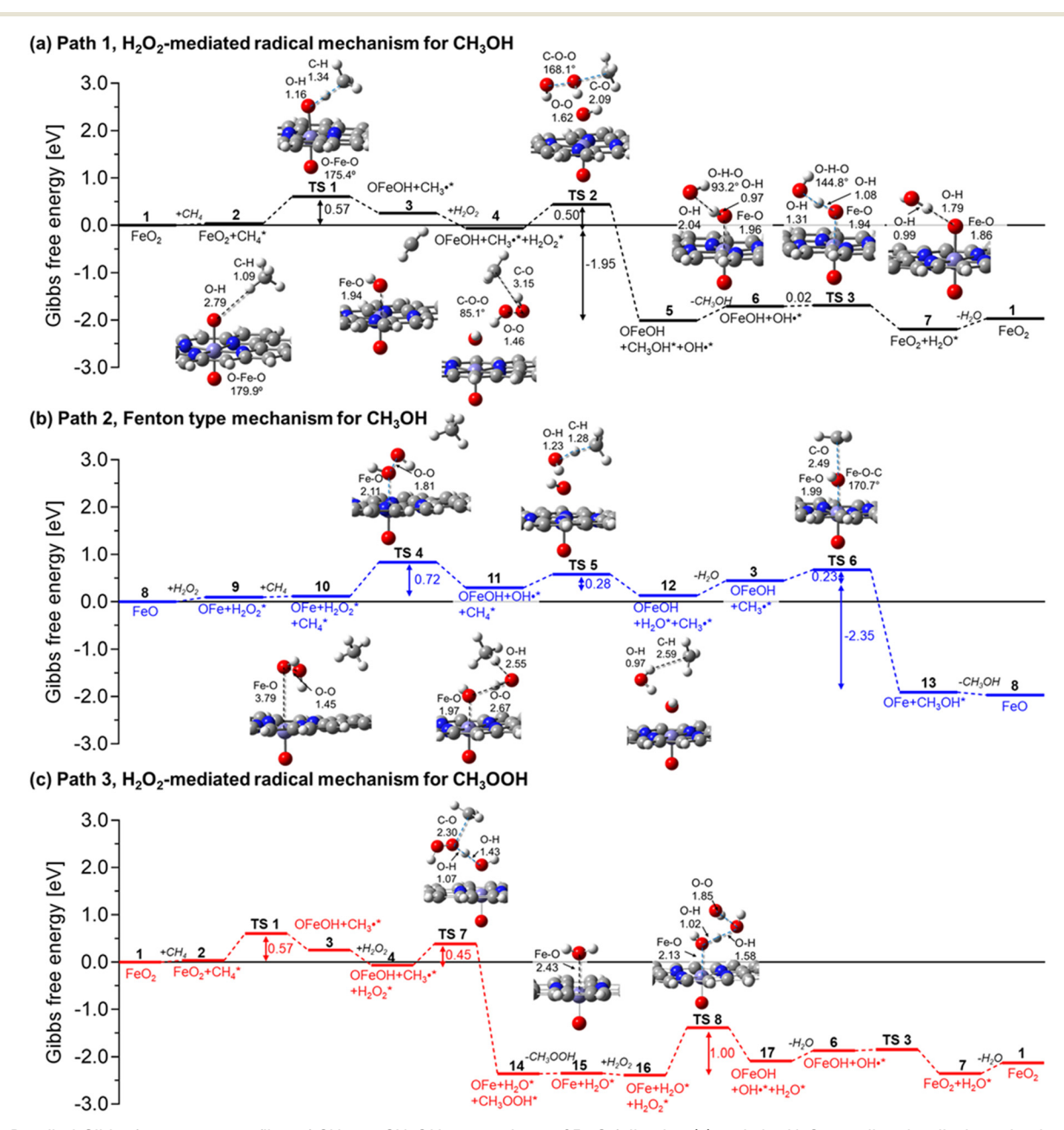


Fig. 2 Detailed Gibbs free energy profiles of CH₄-to-CH₃OH conversion at 25 °C following (a) path 1 – H₂O₂-mediated radical mechanism on the di-oxo center, (b) path 2 - Fenton type mechanism on the mono-oxo center, and (c) path 3 - CH_4 -to- CH_3OOH conversion following H_2O_2 mediated radical mechanism on the di-oxo center. "Fe" on the profiles stands for the FeN_4/GN catalyst structure, and "TS" represents the transition state. Asterisk (*) denotes the adsorbed species on the catalyst surface. Selected interatomic distances (in Å) are shown on the molecular structures.

can emerge from calculations of low-frequency modes.⁵⁷ The studied mechanisms are presented in Fig. 2 (*vide infra*) and in Section S2 of the ESI† file.

Microkinetic model

Paper

The microkinetic model consists of a system of coupled ordinary differential equations, which describe the time-evolution of the concentration of species. The differential equations have the form:

$$\frac{\mathrm{d}c_i}{\mathrm{d}t} = \sum_j \nu_{ij} r_j(\overrightarrow{c}) \tag{2}$$

where c_i is the concentration of species i, r_j is the rate of reaction j, which is a function of concentrations \vec{c} , and v_{ij} is the stoichiometric number of species i in reaction j. For the FeN₄/GN system, 'species' are unique complexes between the Fe-center and some (or none) ligands, which include a single oxygen (mono-oxo center), two oxygens (di-oxo center) and other ligands that appear as intermediates in catalytic cycles. The di-oxo center has an initial concentration of unity as it has been suggested to be an active center.³⁷ The fraction (coverage) of species i (x_i) is defined as the ratio of the number of species i (n_i) to the total number of all the possible species:

$$x_i = \frac{n_i}{\sum_{i} n_i} \tag{3}$$

The mole fractions of all species obey the summation:

$$\sum_{i} x_i = 1 \tag{4}$$

In the case of FeN_4/GN , the entire catalytic cycle is assumed to take place at single Fe-centers, with no interaction or cross-reactions between adjacent Fe-centers. Thus, each elementary reaction is first order, with the forward (backward) reaction rate depending only on the concentration of the reactant (product) species multiplied by the rate constant. The rate constants of reactions are calculated according to transition-state theory as:

$$k = \frac{k_{\rm B}T}{h} \exp\left[-\frac{\Delta G^{\ddagger}}{k_{\rm B}T}\right] \tag{5}$$

where $k_{\rm B}$ is the Boltzmann constant, T is the temperature, and ΔG^{\ddagger} is the standard Gibbs free energy barrier determined using DFT calculations as previously described.

Adsorption of a free species (*e.g.*, CH_4 and H_2O_2) from the solution to the catalyst surface is taken to be purely diffusion-controlled, where the catalyst is assumed to be a stationary 2-D flake, giving the following expression for the adsorption rate constant k_a :⁵⁸

$$k_{\rm a} = 4r_{\rm a}D_ic_i \tag{6}$$

where r_a is the radius of the active site, and D_i and c_i are the diffusivity and the bulk concentration of the adsorbing

species i, respectively. The diffusivity of a free species is obtained by the Stokes–Einstein equation:

$$D_i = \frac{k_{\rm B}T}{6\pi n r_i} \tag{7}$$

where η is the viscosity of the fluid and r_i is the radius of the species. The viscosity of the fluid is approximated by the dynamic viscosity of water at room temperature. The relative radius of the adsorption center of the catalyst to free species is approximated to be 4 (*i.e.*, $r_a = 4r_i$), considering the larger size of the FeN₄ center compared to free molecules. This leads to the adsorption rate constant given by:

$$k_{\rm a} = \frac{8}{3\pi} \frac{k_{\rm B}T}{\eta} c_i \tag{8}$$

Note that the unit of k_a is s⁻¹. The desorption rate constants k_d are calculated from the adsorption rate constant *via* the equilibrium constant K_{eq} :

$$K_{\rm eq} = \frac{k_{\rm a}}{k_{\rm d}} = \exp\left[-\frac{\Delta G}{k_{\rm B}T}\right]$$
 (9)

 ΔG is the free energy change of adsorption. Solving eqn (9) for $k_{\rm d}$ gives:

$$k_{\rm d} = k_{\rm a} \exp\left[\frac{\Delta G}{k_{\rm B}T}\right] \tag{10}$$

Note that k_d (unit s^{-1}) is independent of the bulk concentration of the desorbing species.

The coupled ODEs were solved using a Python 3-based code with the solve_ivp function from the Scipy package⁵⁹ scipy.integrate. The integration intervals were chosen to be long enough (10⁴ seconds in general) to ensure that a steady state is reached.

Degree of rate control (DRC) and degree of selectivity control (DSC) analyses⁶⁰ were performed to identify elementary steps with rate control of the CH₃OH and CH₃-OOH formation and the CH₃OH selectivity. DRC of elementary step i ($X_{RC,i}$) is defined as:

$$X_{\text{RC},i} = \frac{k_i}{r} \left(\frac{\partial r}{\partial k_i} \right)_{k_{j \neq i}, K_i} \tag{11}$$

where k_i is the forward rate constant of step i and r is the overall reaction rate. The $X_{\mathrm{RC},i}$ is approximated with a finite difference method, performed by lowering the forward and backward rate constant of a single elementary step by 1%, while all the other rate constants k_i are unvaried, and observing the change in the overall reaction rate at steady state. A positive $X_{\mathrm{RC},i}$ value indicates a rate-limiting step, whereas a negative value indicates an inhibition step. The degree of selectivity control $X_{\mathrm{SC},i}$ of an elementary step i is defined as:

$$X_{\text{SC},i} = \frac{1}{S} \left(\frac{\partial S}{\partial k_i} \right)_{k_{i \neq i}, K_i} \tag{12}$$

where *S* is the CH₃OH selectivity, which is defined as the ratio of the catalyst's TOF to CH₃OH to the sum of the TOFs to both products.

The reaction orders of CH_3OH and CH_3OOH formation were determined with respect to each reactant (CH_4 and H_2O_2) as calculated from:

$$n_i = \frac{\partial \ln r}{\partial \ln c_i} \tag{13}$$

where r is the net reaction rate and c_i is the concentration of the reactant i. The partial derivatives were approximated by finite differences by increasing c_i by 1%, while all the other parameters were kept constant. Apparent activation energies for CH₃OH and CH₃OOH formation were calculated from the slopes of their respective Arrhenius plots in the temperature range from 278.15 to 318.15 K. This approach is valid as the plots were found to be linear in the tested temperature range. Reaction conditions and parameters used in the MKM are listed in Table 1.

Further details on MKM can be found in the ESI† Section S3 and the assumptions made in the diffusion model are discussed in the ESI† Section S4.

Results and discussion

Methane conversion mechanisms

CH₃OH formation. Prior work⁴⁰ identified 11 different mechanisms of CH₄-to-CH₃OH conversion over FeN₄/GN. Gibbs free energy profiles of some relevant pathways are reproduced here (Fig. 2, S2, and S3†) for completeness and as additional corrections have been made to the Gibbs free energies for higher accuracy (see Computational details). Fig. 2a and b shows two important mechanisms for CH₄-to-CH₃OH conversion with the net reaction:

$$CH_4 + H_2O_2 \rightarrow CH_3OH + H_2O$$
 (rxn. 1)

Path 1 proceeds over the di-oxo species and is an $\rm H_2O_2$ -mediated radical mechanism (Fig. 2a). The di-oxo center breaks a primary C-H bond of CH₄ to generate a methyl radical (CH₃·), which reacts with $\rm H_2O_2$ to give CH₃OH and a hydroxyl radical (OH·). Thereafter, the hydroxyl radical abstracts H from the hydroxyl center to regenerate the di-oxocenter. Path 2 proceeds over the mono-oxo species and is a Fenton-type reaction mechanism (Fig. 2b). The O=O bond of $\rm H_2O_2$ is homolytically dissociated at the bare Fe side of the mono-oxo center (bottom of the structure shown in Fig. 1(a)),

producing a hydroxyl radical and hydroxylating the Fe site. The hydroxyl radical activates CH_4 to CH_3 , which is converted to CH_3OH by abstracting the hydroxyl surface ligand.

Additional mechanisms include one on a di-oxo center (direct radical mechanism as path 4; Fig. S2 \dagger) and two on a mono-oxo center (direct and H_2O_2 -mediated radical mechanisms as path 5 and 6, respectively; Fig. S3 \dagger). These pathways are associated with higher barriers either for the recovery of the active center (path 4) or homolytic C-H dissociation of CH_4 (paths 5 and 6). Importantly, the different reaction mechanisms share some common states. For example, paths 1 and 2 have common state 3 (Fig. 2), which suggests a possibility of a larger reaction network with a dynamic oxidation state of Fe along the reaction coordinate.

CH₃OOH formation. CH₃OOH is another major, experimentally observed, reaction product.37 Thus, we examine reaction mechanisms for CH4 conversion to CH3-OOH on both the di-oxo (path 3 in Fig. 2) and mono-oxo (path 7 in Fig. S3†) centers. The four first elementary steps of path 3 are identical to those in path 1; the dioxo center homolytically dissociates the primary C-H bond of CH₄, and one H₂O₂ is adsorbed on the surface. Thereafter, one H from H₂O₂ is abstracted by the hydroxylated center, and CH3· species is combined with the remaining OOH simultaneously, producing surface water and CH₃OOH (TS7). This radical mechanism resembles the CH₄ conversion by Pd/MoO₃ photocatalyst reported in ref. 63. Next the surface water is dehydrogenated (to OH) by a second H2O2, producing one water molecule and a hydroxyl radical (OH·) as the O=O bond of H2O2 is dissociated (TS8). This step involves the highest activation energy in the pathway ($\Delta G^{\ddagger} = 1.00 \text{ eV}$). The remaining hydroxyl center is further dehydrogenated by OH-, regenerating the di-oxo active center and closing the catalytic cycle. The mono-oxo counterpart of path 3 is path 7 in Fig. S3,† which involves a high activation energy for the C-H bond cleavage (TS10, ΔG^{\ddagger} = 1.52 eV). Hence, substantial formation of CH₃OOH is only possible via path 3. The net reaction of the mechanism is:

$$CH_4 + 2H_2O_2 \rightarrow CH_3OOH + 2H_2O$$
 (rxn. 2)

Table 1 Reaction conditions and parameters for microkinetic modeling

Parameter	Symbol	Value	Units
Standard molarity	c°	1	mol dm ⁻³
H_2O_2 concentration ^a	$[H_2O_2]$	5	mol dm ⁻³
H ₂ O concentration	$[H_2O]$	50	$\mathrm{mol}\;\mathrm{dm}^{-3}$
CH ₄ concentration ^a	$[CH_4]$	0.03	mol dm ⁻³
CH ₃ OH concentration	[CH ₃ OH]	1×10^{-5}	$\mathrm{mol}\;\mathrm{dm}^{-3}$
CH ₃ OOH concentration	[CH ₃ OOH]	1×10^{-5}	$\mathrm{mol}\;\mathrm{dm}^{-3}$
Dynamic viscosity of water	η	890.2 (ref. 61)	μPa s
Henry's constant of CH ₄ in water	$\dot{H}_{\mathrm{CH}_{4}}$	38 741 (ref. 62)	bar

^a Based on the experimental condition.³⁷

There are two important observations on path 3: first, TS7 (producing CH₃OOH) competes with TS2 of path 1 (producing CH₃OH) since they share the reactant state (state 4), where the barrier for CH₃OOH formation is lower than that of CH₃OH formation, which indicates a preference for CH₃OOH formation over the di-oxo center. Second, state 15 (after CH₃OOH has desorbed) is essentially a mono-oxo center with a water molecule on the bare Fe side. If the water desorbs (instead of going through the remaining steps in path 3), then the system is converted to the bare mono-oxo state (state 8). Conversely, if one water molecule adsorbs on the bare Fe site of the mono-oxo catalyst and reacts with H₂O₂ (through TS8), it forms the di-oxo center. These scenarios provide routes to connect different reaction mechanisms on two different active centers. To investigate the possibility of dynamic behavior of the active center, the additional elementary step of water adsorption on the bare Fe site of the mono-oxo center is considered in the MKM.

Microkinetic modeling

Reaction network. We carried out MKM calculations with the parameters in Table 1 using either the full reaction mechanism or a reduced set of the reaction mechanisms. For the full reaction mechanism, all the reaction pathways on both the di- and mono-oxo centers (i.e., paths 1-7) are considered. For the reduced set of reaction mechanisms, only three energetically feasible mechanisms (i.e., paths 1-3) were included. The differences of the total TOFs between the full reaction mechanisms and the reduced set of the reaction mechanisms are negligible owing to the high barriers in paths 4-7 (see ESI† Section S3). Hence, the reduced model is used in the present work for convenience to analyze the kinetic behaviour. The elementary reactions included in the reduced model are tabulated in Table 2.

Table 2 shows the states and elementary steps that are shared by different reaction pathways. The elementary steps that include different pathways allow for the construction of a nested reaction network, as visualized in Fig. 3. The reaction network is composed of the full pathways of paths 1 and 2 and a part of path 3. The rest of the steps of path 3 (from state 15 to 6) are presented as a dotted line in Fig. 3 with the details being omitted due to the net small negative steady-state reaction rates (R17-19 in Table 2). The arrow width indicates magnitude of elementary reaction rates at steady state (Table 2). Fig. 3 shows a catalytic cycle with a high TOF that emerges from the construction of the nested network: starting from a mono-oxo center (state 8; upper right), (1) methyl radical is formed following path 2 (from state 8 to 3; blue arrows), (2) CH₃OOH is formed following the steps identified in path 3 (from state 3 to 15; red arrows), and (3) the mono-oxo center is regenerated as a surface water molecule desorbs (R20). The product of this catalytic cycle is CH₃OOH, with the net reaction being that of rxn. (2). In the cycle, the oxidation state of Fe changes between +4 and +5 (Fig. 3). CH₃OH can be produced either via a reaction between methyl radical and hydroxyl center (R13 through TS6, i.e., completing path 2) or following the full path 1 from

Table 2 Steady-state net reaction rates of all elementary steps in the reduced set of the reaction mechanisms calculated by MKM at 25 °C and reaction conditions tabulated in Table 1

	Elementary step ^a	$Step^b$	Net rate ^{c} (s ⁻¹)	Starting state	Ending state	Pathway
R1	$FeO_2 + CH_4 \rightarrow FeO_2 + CH_4^*$	Ads	1.70×10^{-7}	1	2	1, 3
R2	$FeO_2 + CH_4^* \rightarrow OFeOH + CH_3 \cdot *$	TS1	1.70×10^{-7}	2	3	1, 3
R3	$OFeOH + CH_3 \cdot * + H_2O_2 \rightarrow OFeOH + CH_3 \cdot * + H_2O_2^*$	Ads	1.47×10^{-6}	3	4	1, 3
R4	$OFeOH + CH_3 \cdot * + H_2O_2^* \rightarrow OFeOH + CH_3OH^* + OH \cdot *$	TS2	1.75×10^{-7}	4	5	1
R5	OFeOH + $CH_3OH^* + OH^{**} \rightarrow OFeOH + CH_3OH + OH^{**}$	Des	1.75×10^{-7}	5	6	1
R6	$OFeOH + OH \cdot * \rightarrow FeO_2 + H_2O*$	TS3	1.70×10^{-7}	6	7	1, 3
R7	$FeO_2 + H_2O^* \rightarrow FeO_2 + H_2O$	Des	1.70×10^{-7}	7	1	1, 3
R8	$\text{FeO} + \text{H}_2\text{O}_2 \rightarrow \text{OFe} + \text{H}_2\text{O}_2^*$	Ads	1.39×10^{-6}	8	9	2
R9	$OFe + H_2O_2^* + CH_4 \rightarrow OFe + H_2O_2^* + CH_4^*$	Ads	1.39×10^{-6}	9	10	2
R10	$OFe + H_2O_2^* + CH_4^* \rightarrow OFeOH + OH \cdot * + CH_4^*$	TS4	1.39×10^{-6}	10	11	2
R11	$OFeOH + OH^* + CH_4^* \rightarrow OFeOH + H_2O^* + CH_3^*$	TS5	1.39×10^{-6}	11	12	2
R12	OFeOH + H_2O^* + $CH_3\cdot^*$ \rightarrow OFeOH + H_2O + $CH_3\cdot^*$	Des	1.39×10^{-6}	12	3	2
R13	OFeOH + $CH_3 \cdot * \rightarrow OFe + CH_3OH*$	TS6	9.37×10^{-8}	3	13	2
R14	$OFe + CH_3OH^* \rightarrow FeO + CH_3OH$	Des	9.37×10^{-8}	13	8	2
R15	$OFeOH + CH_3 \cdot * + H_2O_2^* \rightarrow OFe + H_2O^* + CH_3OOH^*$	TS7	1.30×10^{-6}	4	14	3
R16	$OFe + H_2O^* + CH_3OOH^* \rightarrow OFe + H_2O^* + CH_3OOH$	Des	1.30×10^{-6}	14	15	3
R17	$OFe + H_2O^* + H_2O_2 \rightarrow OFe + H_2O^* + H_2O_2^*$	Ads	-5.96×10^{-8}	15	16	3
R18	$OFe + H_2O^* + H_2O_2^* \rightarrow OFeOH + OH^* + H_2O^*$	TS8	-4.96×10^{-9}	16	17	3
R19	OFeOH + OH·* + $H_2O^* \rightarrow OFeOH + OH·* + H_2O$	Des	-4.96×10^{-9}	17	6	3
R20	$OFe + H_2O^* \rightarrow FeO$	Des	1.30×10^{-6}	15	8	2, 3

^a Asterisk (*) denotes the adsorbed species on the Fe-center. ^b "Ads" and "Des" represent adsorption and desorption steps, respectively, and "TS#" stands for the transition state involved in the reaction step. c A negative reaction rate indicates that the backward reaction is faster than the forward reaction.

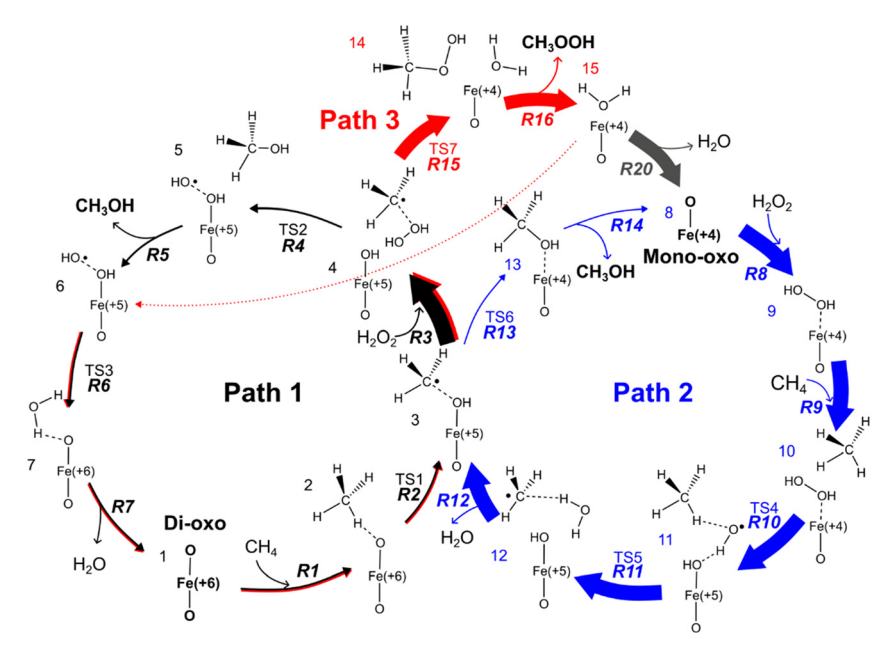


Fig. 3 Reaction network of CH_4 conversion to CH_3OH and CH_3OOH . The arrow width indicates the relative steady-state reaction rate of each elementary step estimated by MKM. "Fe" on each structure stands for the FeN_4/GN catalyst with the corresponding formal oxidation state of Fe in parenthesis. The reaction labels correspond to the reactions in Table 2 and the color scheme for each pathway is consistent with Fig. 2. Mono-oxo and di-oxo denote the two different states of the catalyst involved in the catalytic cycles and serve as starting points on the nested reaction network.

state 4. The latter involves di-oxo catalyst with the high oxidation state of Fe (+6). The Fe oxidation state changes between +4 and +6, as suggested in our previous work.³⁷

Fig. 4 shows the time evolution of the site distribution and TOFs. The initial di-oxo site (with one H_2O molecule adsorbed; state 7) is gradually converted to mono-oxo (with adsorbates on the bare Fe site: one H_2O molecule – state 15, or both H_2O and H_2O_2 molecules – state 16) over time (Fig. 4a). The conversion of the di-oxo state to the mono-oxo

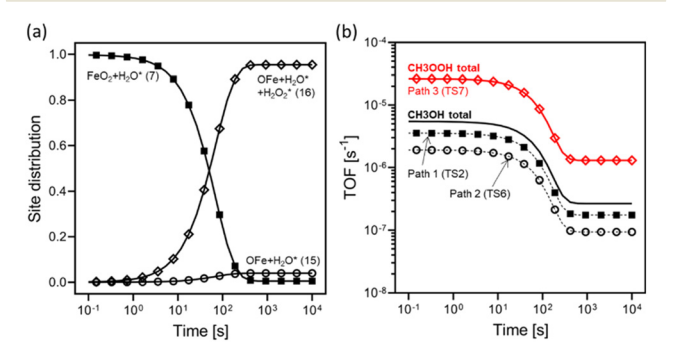


Fig. 4 Change of (a) the distribution of the catalytic site and (b) turnover frequency (TOF) over time up to 10^4 s determined by microkinetic modeling (MKM) using a reduced reaction system (paths 1–3) at 25 °C and reaction conditions tabulated in Table 1. On panel (b), the TOF to each product (thick solid lines) is determined as a sum of the rates of the product desorption steps. The TOFs through individual pathways (dotted lines with symbols) represented by reaction rates of their characteristic elementary steps as shown in the parentheses. See ESI† Section S3 for the results with a full reaction system (paths 1–7).

state is reasonable given the higher thermodynamic stability of mono-oxo over di-oxo³⁷ and the high barrier for di-oxo regeneration ($\Delta G^{\ddagger} = 1.00$ eV; TS8 in Fig. 2c). The conversion of di-oxo accelerates after ~10 s and there is a clear switchover from a di-oxo-dominated to a mono-oxo-dominated Fe population at around 50 s. Di-oxo Fe sites have almost completely disappeared at around 400 s.

The TOFs towards both CH_3OH and CH_3OOH production decrease with time: from $5 \times 10^{-6} \, \mathrm{s}^{-1}$ to $3 \times 10^{-7} \, \mathrm{s}^{-1}$ for CH_3OOH and from $3 \times 10^{-5} \, \mathrm{s}^{-1}$ to $1 \times 10^{-6} \, \mathrm{s}^{-1}$ for CH_3OOH (Fig. 4b). The time evolution of the TOFs is linked to the switchover of the site distribution from di-oxo to mono-oxo. Thus, the di-oxo center is more active than the mono-oxo center for both products but is eventually consumed due to the unfavorable thermodynamics and kinetics of its regeneration. The reaction rates of the individual pathways are shown in Fig. 4b (TS2, TS6, and TS7 characterize paths 1, 2, and 3, respectively; see Fig. 2 for details). The rate of path 3 is identical to the TOF to CH_3OOH as path 3 is the only pathway where CH_3OOH is formed. By contrast, CH_3OH is formed from both paths 1 and 2. The contribution from path 1 is roughly 2 times of that of path 2 (Fig. 4b).

Four C1 products have been reported experimentally:³⁷ CH₃OH, CH₃OOH, HCOOH, and HOCH₂OOH. Cui *et al.*³⁷ proposed that the last two products are produced by oxidation of CH₃OH. However, the possibility of CH₃OOH oxidation to these products cannot be ruled out. Wang *et al.* demonstrated the room-temperature activity of FeN₄/GN towards C₂H₆ activation, showing that the –OOH derivative (CH₃CH₂OOH) can be further converted to a carboxylic acid

(CH₃COOH).⁶⁴ A direct comparison of experimental and simulated selectivities is difficult as we do not explore further oxidation of CH₃OH and CH₃OOH. Nevertheless, assuming identical consumption rates of CH3OH and CH3OOH (to HCOOH, and HOCH2OOH), the experimental CH3OH selectivity is 11% (the amount of CH₃OH divided by the amount of CH₃OH + CH₃OOH produced over 10 hours).³⁷ This is in a good agreement with the MKM-determined CH₃-OH selectivity, which is 17% (Fig. 4b). It should be noted that the product selectivity is sensitive to the adsorption rate constant (k_a) . To study the effect of k_a , the time evolution of the site distribution and TOF are simulated with lower and higher adsorption rate constants (ESI† Section S4 and Fig. S7). The active site distribution and the total TOF do not depend on k_a . However, the CH₃OH selectivity changes to 13% and 29% with 4 times higher and 4 times smaller k_a than the original k_a (eqn (8)), respectively. This result shows a possible relationship between product selectivity and diffusion (see eqn (6)) that is independent of the overall CH₄ conversion by the FeN₄/GN catalyst. The CH₃OH selectivity control strategy by limiting diffusion process has also been suggested by Nørskov et al.38

Degree of rate and selectivity control. DRC $(X_{RC,i})$ and DSC $(X_{\text{SC}.i})$ analyses⁶⁰ are shown in Fig. 5. For both products, 6 elementary steps are found to have rate control, namely R2, R3, R4, R10, R13, and R15 (Table 2). Among these steps, R10 is found to have the largest rate control with $X_{\rm RC} = 0.88-0.89$ for both products over the temperature range (278-318 K). R10 is the dissociation of O=O bond in H_2O_2 on the bare Fe side of the mono-oxo center (TS4; see Fig. 2b). It has the highest activation energy (0.72 eV) in the most favorable pathway identified in Fig. 3 (bold arrows). This step has equivalent influences on both products (CH3OH and CH3-OOH), and therefore there is no net effect on the product selectivity (i.e., $X_{SC} = 0$) as seen in Fig. 5c. Similarly, R2 has no effect on the selectivity since it has the same effect on both products with a smaller $X_{\rm RC}$ than that of R10 (0.10-0.12). R2 and R10 have no selectivity control since they are associated with the production of states that are shared by both products. As shown in the reaction network in Fig. 3, starting from the mono-oxo species (state 8; upper right), the reaction proceeds through a single pathway up to state 3. Hence, all the elementary reaction steps that produce any state between states 8 and 3 have a net zero effect on the product selectivity.

For CH₃OH production, R4 and R15 are equivalently the second most influential steps with similar DRC values but opposite sign (blue lines in Fig. 5a): $X_{RC,R4} > 0$ (rate-limiting) and $X_{RC,R15}$ < 0 (inhibition). The CH₃OH formation rate is, thus, accelerated and slowed down by increasing the rates of R4 and R15, respectively. They have opposite effects as they occur in parallel at the shared state 4, leading to the production of either CH₃OH (R4) or CH₃OOH (R15) (Fig. 3). Thus, the signs of $X_{RC,R4}$ and $X_{RC,R15}$ are exchanged for CH₃-OOH compared to CH_3OH (Fig. 5b). The magnitudes of X_{RC} of R4 and R15 for CH₃OOH are smaller as the overall TOF to CH₃OOH is much higher than that of CH₃OH (Fig. 4b). Consequently, these steps play a significant role in product selectivity (Fig. 5c). Similarly, there are two reaction steps that are the third most influential, R3 and R13 (red lines in Fig. 5): $X_{RC,R13} > 0$ (rate-limiting) and $X_{RC,R3} < 0$ (inhibition). With increasing temperature (from 278.15 to 318.15 K), R4 and R15 become less influential (smaller absolute values of X_{RC}), whereas R3 and R13 become more influential (larger absolute values of X_{RC}). Hence, all these steps show a significant X_{SC} at a high temperature. Again, the DRC and DSC of these elementary steps (Fig. S8†) strongly depends on the adsorption rate constant (k_a) , primarily because it determines the rate of R3 (H₂O₂ adsorption step). See ESI[†] Section S4 for further details.

Temperature effect. To understand how the reaction kinetics depend on temperature, we investigate how the TOF changes over time by varying the temperature between 278.15 and 318.15 K as shown in Fig. 6. As expected, TOFs to both products increase with temperature. The steady-state TOFs to CH₃OH and CH₃OOH increase by roughly an order of magnitude as the temperature shifts from 298.15 K to 318.15 K. On the other hand, the low-temperature (278.15 K) steady-

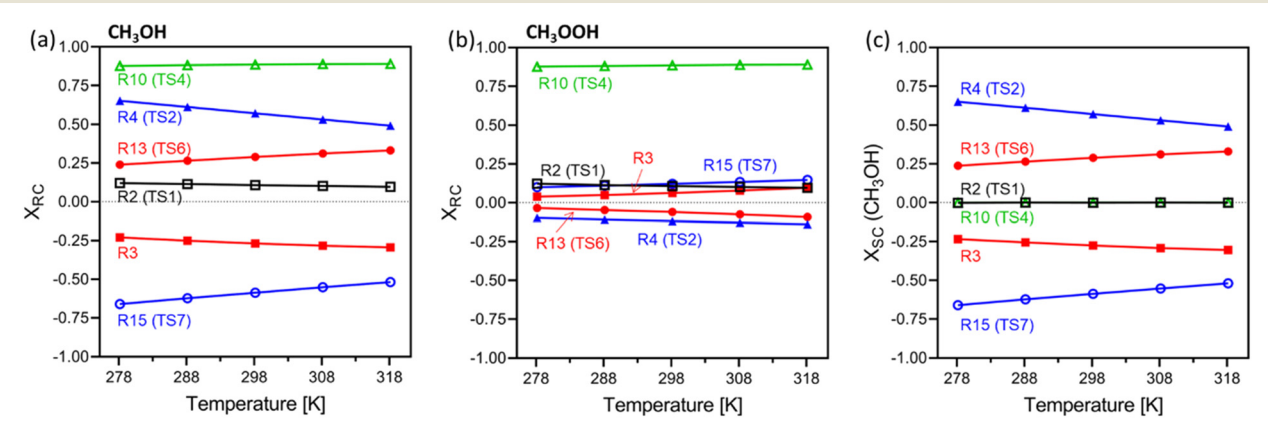


Fig. 5 Degree of rate control (X_{RC}) for (a) CH₃OH and (b) CH₃OOH, and (c) degree of selectivity control (X_{SC}) of CH₃OH. The elementary steps that compete are shown with the same color. Details of the elementary steps are found in Table 2. The elementary steps with the absolute value of $X_{\rm RC}$ lower than 2.0 × 10⁻³ over the studied temperature range are omitted.

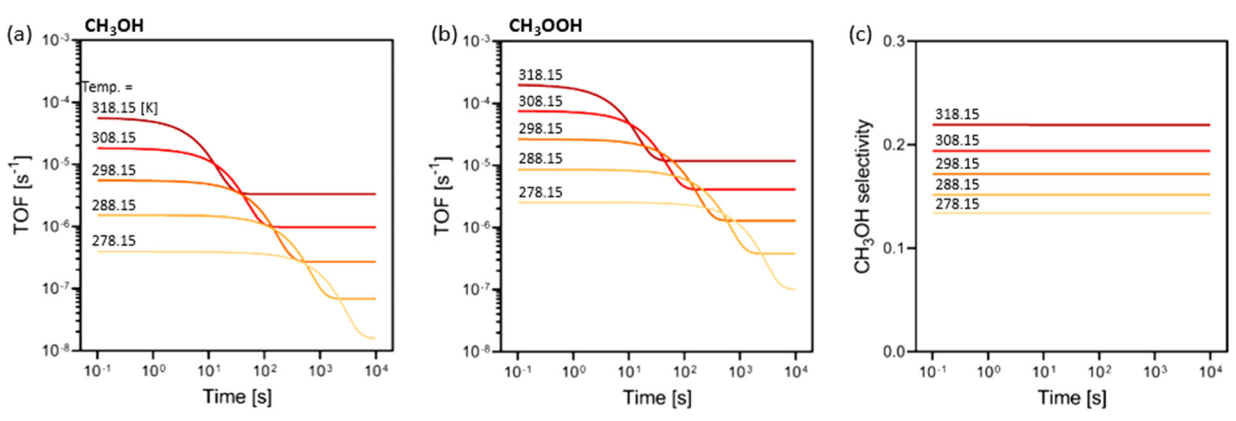


Fig. 6 TOFs to (a) CH₃OH and (b) CH₃OOH, and (c) CH₃OH selectivity under various temperatures between 278.15 and 318.15 K over time up to 10⁴ s.

state TOFs to CH₃OH and CH₃OOH are only 6 and 8% of those at 298.15 K. Interestingly, the TOF to CH₃OH increases more significantly compared to CH₃OOH as temperature increases. This leads to an increase in CH₃OH selectivity with temperature, from 13% (at 278.15 K) to 22% (at 318.15 K) (see Fig. 5c). This clearly demonstrates that temperature not only modifies the overall reaction rate but also controls product selectivity, where a small increase in temperature leads to higher TOF to CH4 and higher selectivity toward CH₃OH. Nevertheless, it should be noted that an increase in temperature can also potentially lead to over-oxidation to CO₂, which cannot be assessed in the present model.

Apparent activation energy and reaction order analysis. Based on the temperature dependent steady-state TOFs to CH₃OH and CH₃OOH (Fig. 6a and b), we produce the Arrhenius plots shown in Fig. 7a. In the given temperature range, the apparent activation energies ($\Delta E_{\text{app.}}^{\ddagger}$) for CH₃OH and CH₃OOH are 1.06 and 0.94 eV, respectively. The apparent activation energy can also be calculated from the degree of rate control and relative Gibbs free energies of each step as reported by Mao and Campbell.65 Considering only the 6 elementary steps reported in Fig. 5 with an ideal behavior assumption (i.e., neglecting effects of adsorbing/desorbing species and catalytic site fractions), $\Delta E_{\text{app.}}^{\ddagger} = 1.07 - 1.09 \text{ eV for}$

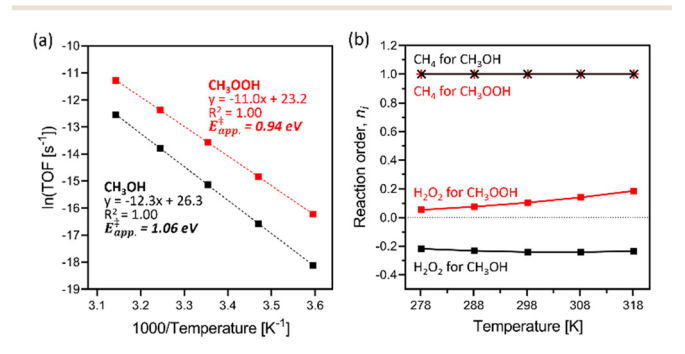


Fig. 7 (a) Arrhenius plots for the production of CH₃OH (black) and CH₃OOH (red) with linear fits and apparent activation energies ($\Delta E_{\rm app}^{\ddagger}$). (b) Reaction order of reactants (CH₄ and H₂O₂) for each product.

CH₃OH and 0.88-0.84 eV for CH₃OOH, which are increasing and decreasing with temperature (from 278.15 to 318.15 K), respectively. Both results agree with the higher TOF of CH₃-OOH than that of CH₃OH reported in Fig. 4.

The reaction orders, n_i , of the reactants (CH₄ and H₂O₂) with respect to each product (CH3OH and CH3OOH) obtained by eqn (13) are presented in Fig. 7b. Reaction rates of both products depend linearly on [CH₄] over the temperature range investigated (i.e., $n_{\rm CH_4}$ = 1). On the contrary, $n_{\rm H_2O_2}$ is smaller for both products; around -0.23 for CH₃OH and 0.06-0.19 for CH₃OOH and increasing with temperature. Thus, increased [H2O2] yields slower CH3OH formation and faster CH₃OOH formation. The reason for the different signs of the H_2O_2 reaction order is that R3 (H_2O_2 adsorption) outcompetes the parallel reaction, R13 (see Fig. 3). Although the rate of the minor reaction stream to form CH₃OH after state 4 increases as the rate of R3 increases, the decrease in the rate of R13 counteracts this effect, leading to a net decrease in CH3OH formation rate. Thus, the product selectivity can be controlled by modifying [H₂O₂], where low [H₂O₂] favors high CH₃OH selectivity.

It is worth noting that the difference between $n_{H_2O_2}$ for the two products increases with temperature. This indicates that selectivity control by [H2O2] is more significant at a higher temperature, as also seen in Fig. 5c (red lines; R3 is adsorption of H₂O₂ from bulk phase to catalyst).

The apparent activation energies and reaction orders have been also investigated with different adsorption rate constants (k_a) (Fig. S9†). The analysis shows that varying k_a has a small effect on the overall activity (nearly constant $\Delta E_{\text{app.}}^{\ddagger}$) but significantly affects $n_{\text{H}_2\text{O}_2}$ in such a way that the lower k_a results to higher magnitude of $n_{H_2O_2}$. The selectivity control by [H₂O₂] can, thus, be facilitated by slowing down the diffusion. In addition, as already mentioned, the CH₃OH selectivity increases with temperature (Fig. 6c). Taken all together, we demonstrate the synergistic effects among temperature, [H₂O₂], and diffusion on controlling product selectivity, where the CH₃OH selectivity can be enhanced by reaction conditions with high temperature, low [H2O2], and slow diffusion. This provides a large design space for roomtemperature CH_4 conversion by a FeN_4/GN catalyst towards target liquid product.

Conclusions

We developed a first-principles-based mean-field microkinetic model (MKM) for partial CH₄ conversion to CH₃OH and CH₃-OOH over FeN₄/GN. In total, 7 reaction mechanisms (5 for CH₃OH and 2 for CH₃OOH) on two different Fe-centers (i.e., di-oxo and mono-oxo) are considered. A reaction network is constructed, which involves a dynamic change of the Fe oxidation state between +4, +5 and +6. The evolution of the site fraction shows that the di-oxo site is converted to the mono-oxo site over time. The switchover from di-oxo to mono-oxo is connected to a significant drop in turnover frequency (TOF). Thus, the di-oxo center (Fe⁶⁺) is more active but less stable compared to the mono-oxo center (Fe⁴⁺). The catalytic activity for CH3OH formation can, therefore, be enhanced by stabilizing the metal center in the di-oxo form. CH₃OH and CH₃OOH are found to be minor and major reaction products, respectively. The CH3OH selectivity is found to be 17%, which agrees with the experimental observations.³⁷ The degree of rate control analysis shows that scission of the O=O bond in H₂O₂ is rate-controlling. Interestingly, however, this step has no net effect on product selectivity. Instead, two pairs of competing elementary reaction steps with significant influences on the product selectivity are identified by the degree of selectivity analysis. The apparent activation energies obtained from Arrhenius plots are consistent with the fact that CH₃OOH is the major product. The apparent activation energy for CH₃OOH is calculated to be 0.94 eV, whereas the value is 1.06 eV for CH₃OH.

Three key factors for product selectivity control are identified: temperature, H2O2 concentration, and diffusion. Increasing temperature accelerates the overall TOF as expected. As the CH₃OH formation rate has a stronger temperature dependence than CH₃OOH formation, the CH₃-OH selectivity can be enhanced by increasing the temperature. The reaction order analysis demonstrates the opposite effect of [H₂O₂] on the product distribution. The CH₃OH production is favored by a lower [H₂O₂]. Furthermore, the diffusion of free species from bulk phase to a catalyst surface is found to play a significant role in the reaction kinetics by altering product selectivity without affecting the overall CH4 conversion. More importantly, we reveal that there is a synergistic effect among these factors as they have a mutual dependence. This suggests a significant engineering space exists for product selectivity in CH₄ conversion by FeN₄/GN catalyst.

Generally, we demonstrated that the DFT-based kinetic modeling is a useful tool for investigating complicated reaction systems like that of methane to methanol conversion. Our findings provide an in-depth kinetic understanding of the low-temperature $\mathrm{CH_4}$ conversion to C1 products, which can potentially guide experimental efforts to

discover efficient catalysts, as well as fine-tune catalytic performance.

Author contributions

The project was conceptualized and supervised by G. M. and H. G. Computational chemistry calculations were performed by S. H. Microkinetic modeling was performed by M. M. K. and S. H. in cooperation with E. V. M. The original draft of the manuscript was prepared by S. H., M. M. K., G. M. and H. G. All authors contributed to scientific discussions and editing of the manuscript.

Conflicts of interest

There are no conflicts to declare.

Acknowledgements

This material is based upon work supported by the National Science Foundation (NSF) under Grant No. 1920623. GM acknowledges sabbatical support from Chalmers University of Technology, Areas of Advance: Materials Science, and the Wenner Gren Foundation. M. M. K. and H. G. acknowledge support from the Knut and Alice Wallenberg Foundation (KAW 2015.0058) and the Swedish Research Council (2020-05191). The Competence Centre for Catalysis (KCK) is hosted by Chalmers University of Technology and financially supported by the Swedish Energy Agency (52689-1) and the member companies Johnson Matthey, Perstorp, Powercell, Preem, Scania CV, Umicore and Volvo Group. This research was supported in part by the University of Pittsburgh Center for Research Computing, RRID:SCR_022735, through the resources provided. Specifically, this work used the H2P cluster, which is supported by NSF award number OAC-2117681.

References

- 1 BP Statistical Review of World Energy 2021, BP p.l.c., London,
- 2 Carbon Dioxide Emissions Coefficients by Fuel, U.S. Energy Information Administration, https://www.eia.gov/ environment/emissions/co2_vol_mass.php, (accessed April 2023).
- 3 A. Moumen, G. Azizi, K. B. Chekroun and M. Baghour, *Int. J. Glob. Warm.*, 2016, **9**(2), 229–253.
- 4 2023 Global Gas Flaring Tracker Report, Global Gas Flaring Reduction Partnership, Washington, DC: World Bank Publications, https://thedocs.worldbank.org/en/doc/5d5c5c8b0f451b472e858ceb97624a18-0400072023/original/2023-Global-Gas-Flaring-Tracker-Report.pdf, (accessed April 2023).
- 5 A. P. E. York, T. Xiao and M. L. H. Green, *Top. Catal.*, 2003, 22(3-4), 345-358.
- 6 H. D. Gesser, N. R. Hunter and C. B. Prakash, *Chem. Rev.*, 1985, **85**(4), 235–244.

- 7 J. R. Rostrup-Nielsen, J. Sehested and J. K. Nørskov, Adv. Catal., 2002, 47, 65-139.
- 8 S. Verhelst, J. W. G. Turner, L. Sileghem and J. Vancoillie, Prog. Energy Combust. Sci., 2019, 70, 43-88.
- 9 A. Hamnett, Catal. Today, 1997, 38(4), 445-457.
- 10 S. Wasmus and A. Küver, J. Electroanal. Chem., 1999, 461(1-2), 14-31.
- 11 G. J. Hatchings, C. P. Nicolaides and M. S. Scurrell, Catal. Today, 1992, 15(1), 23-49.
- 12 F. Yaripour, F. Baghaei, I. Schmidt and J. Perregaard, Catal. Commun., 2005, 6(2), 147-152.
- 13 T. Waters, R. A. J. O'Hair and A. G. Wedd, J. Am. Chem. Soc., 2003, 125(11), 3384-3396.
- 14 M. Ravi, M. Ranocchiari and J. A. van Bokhoven, Angew. Chem., Int. Ed., 2017, 56(52), 16464-16483.
- 15 R. H. Crabtree, Chem. Rev., 1995, 95, 987-1007.
- 16 P. Kumar, T. A. Al-Attas, J. Hu and M. G. Kibria, ACS Nano, 2022, 16(6), 8557-8618.
- 17 N. Aristov and P. B. Armentrout, J. Phys. Chem., 1987, 91, 6178-6188.
- 18 Y.-M. Chen, D. E. Clemmer and P. B. Armentrout, J. Am. Chem. Soc., 1994, 116, 7815-7826.
- 19 D. Schröder, H. Schwarz, D. E. Clemmer, Y. Chen, P. B. Armentrout, V. I. Baranov and D. K. Böhme, Int. J. Mass Spectrom. Ion Processes, 1997, 161(1-3), 175-191.
- 20 A. E. Shilov and G. B. Shul'pin, Chem. Rev., 1997, 97(8), 2879-2932.
- 21 S. Shaik, D. Danovich, A. Fiedler, D. Schröder and H. Schwarz, Helv. Chim. Acta, 1995, 78(6), 1393-1407.
- 22 K. Yoshizawa, Y. Shiota and T. Yamabe, J. Chem. Phys., 1999, 111, 538-545.
- 23 E. E. Claveau, S. Sader, B. A. Jackson, S. N. Khan and E. Miliordos, Phys. Chem. Chem. Phys., 2023, 5313-5326.
- 24 R. A. Periana, D. J. Taube, E. R. Evitt, D. G. Löffler, P. R. Wentreek, G. Voss and T. Masuda, Science, 1993, 259(5093), 340-343.
- 25 R. A. Periana, D. J. Taube, S. Gamble, H. Taube, T. Satoh and H. Fujii, Science, 1998, 280(5363), 560-564.
- 26 H. Dalton, Catal. Today, 1992, 13(2-3), 455-461.
- 27 J. D. Lipscomb, Annu. Rev. Microbiol., 1994, 48, 371-399.
- 28 M.-H. Baik, M. Newcomb, R. A. Friesner and S. J. Lippard, Chem. Rev., 2003, 103(6), 2385-2420.
- S. Sirajuddin and A. C. Rosenzweig, Biochemistry, 2015, 54(14), 2283-2294.
- 30 K. A. Dubkov, V. I. Sobolev, E. P. Talsi, M. A. Rodkin, N. H. Watkins, A. A. Shteinman and G. I. Panov, J. Mol. Catal. A: Chem., 1997, 123(2-3), 155-161.
- 31 G. I. Panov, A. K. Uriarte, M. A. Rodkin and V. I. Sobolev, Catal. Today, 1998, 41(4), 365-385.
- 32 E. V. Starokon, M. V. Parfenov, S. S. Arzumanov, L. V. Pirutko, A. G. Stepanov and G. I. Panov, J. Catal., 2013, 300,
- 33 M. H. Groothaert, P. J. Smeets, B. F. Sels, P. A. Jacobs and R. A. Schoonheydt, J. Am. Chem. Soc., 2005, 127(5), 1394-1395.

- 34 H. A. Doan, Z. Li, O. K. Farha, J. T. Hupp and R. O. Snurr, Catal. Today, 2018, 312, 2-9.
- 35 S. Grundner, M. A. C. Markovits, G. Li, M. Tromp, E. A. Pidko, E. J. M. Hensen, A. Jentys, M. Sanchez-Sanchez and J. A. Lercher, Nat. Commun., 2015, 6, 7546.
- 36 M. V. Parfenov, E. V. Starokon, L. V. Pirutko and G. I. Panov, J. Catal., 2014, 318, 14-21.
- 37 X. Cui, H. Li, Y. Wang, Y. Hu, L. Hua, H. Li, X. Han, Q. Liu, F. Yang, L. He, X. Chen, Q. Li, J. Xiao, D. Deng and X. Bao, Chem, 2018, 4, 1902-1910.
- 38 A. A. Latimer, A. Kakekhani, A. R. Kulkarni and J. K. Nørskov, ACS Catal., 2018, 8(8), 6894-6907.
- 39 C. Hammond, M. M. Forde, M. H. Ab Rahim, A. Thetford, Q. He, R. L. Jenkins, N. Dimitratos, J. A. Lopez-Sanchez, N. F. Dummer, D. M. Murphy, A. F. Carley, S. H. Taylor, D. J. Willock, E. E. Stangland, J. Kang, H. Hagen, C. J. Kiely and G. J. Hutchings, Angew. Chem., Int. Ed., 2012, 51(21), 5129-5133.
- 40 S. Hong and G. Mpourmpakis, Catal. Sci. Technol., 2021, 11, 6390-6400.
- 41 S. Kozuch and S. Shaik, Acc. Chem. Res., 2011, 44(2), 101-110.
- 42 C. V. Ovesen, B. S. Clausen, B. S. Hammershøi, G. Steffensen, T. Askgaard, I. Chorkendorff, J. K. Nørskov, P. B. Rasmussen, P. Stoltze and P. Taylor, J. Catal., 1996, 158(1), 170-180
- 43 L. C. Grabow, A. A. Gokhale, S. T. Evans, J. A. Dumesic and M. Mavrikakis, J. Phys. Chem. C, 2008, 112(12), 4608-4617.
- 44 K. Reuter, Catal. Lett., 2016, 146, 541-563.
- 45 M. M. Kauppinen, M. M. Melander, A. S. Bazhenov and K. Honkala, ACS Catal., 2018, 8(12), 11633-11647.
- 46 A. H. Motagamwala and J. A. Dumesic, Chem. Rev., 2020, 121(2), 1049-1076.
- 47 Y. Feng, X. Wang, T. V. W. Janssens, P. N. R. Vennestrøm, J. Jansson, M. Skoglundh and H. Grönbeck, ACS Catal., 2021, 11(23), 14395-14407.
- 48 M. Kauppinen, A. Posada-Borbon and H. Grönbeck, J. Phys. Chem. C, 2022, 126(36), 15235-15246.
- 49 M. Abdelgaid, E. V. Miu, H. Kwon, M. M. Kauppinen, H. Grönbeck and G. Mpourmpakis, Catal. Sci. Technol., 2023, 13, 3527-3536.
- 50 M. J. Frisch, G. W. Trucks, H. B. Schlegel, G. E. Scuseria, M. A. Robb, J. R. Cheeseman, G. Scalmani, V. Barone, B. Mennucci, G. A. Petersson, H. Nakatsuji, M. Caricato, X. Li, H. P. Hratchian, A. F. Izmaylov, J. Bloino, G. Zheng, J. L. Sonnenberg, M. Hada, M. Ehara, K. Toyota, R. Fukuda, J. Hasegawa, M. Ishida, T. Nakajima, Y. Honda, O. Kitao, H. Nakai, T. Vreven, J. A. Montgomery Jr., J. E. Peralta, F. Ogliaro, M. Bearpark, J. J. Heyd, E. Brothers, K. N. Kudin, V. N. Staroverov, R. Kobayashi, J. Normand, K. Raghavachari, A. Rendell, J. C. Burant, S. S. Iyengar, J. Tomasi, M. Cossi, N. Rega, J. M. Millam, M. Klene, J. E. Knox, J. B. Cross, V. Bakken, C. Adamo, J. Jaramillo, R. Gomperts, R. E. Stratmann, O. Yazyev, A. J. Austin, R. Cammi, C. Pomelli, J. W. Ochterski, R. L. Martin, K. Morokuma, V. G. Zakrzewski, G. A. Voth, P. Salvador, J. J. Dannenberg, S.

- Dapprich, A. D. Daniels, O. Farkas, J. B. Foresman, J. V. Ortiz, J. Cioslowski and D. J. Fox, *Gaussian 09 (Revision D.01)*, Gaussian Inc., Wallingford, CT, 2014.
- 51 A. D. Becke, J. Chem. Phys., 1992, 96, 2155-2160.
- 52 C. Lee, W. Yang and R. G. Parr, *Phys. Rev. B: Condens. Matter Mater. Phys.*, 1988, 37, 785.
- 53 C. Gonzalez and H. B. Schlegel, *J. Chem. Phys.*, 1989, **90**, 2154–2161.
- 54 V. Barone and M. Cossi, *J. Phys. Chem. A*, 1998, **102**(11), 1995–2001.
- 55 R. A. Alberty, J. Chem. Thermodyn., 2006, 38(4), 396-404.
- 56 O. J. Conquest, T. Roman, A. Marianov, A. Kochubei, Y. Jiang and C. Stampfl, *J. Chem. Theory Comput.*, 2021, 17(12), 7753–7771.
- 57 N. L. Haworth, Q. Wang and M. L. Coote, *J. Phys. Chem. A*, 2017, 121(27), 5217–5225.
- 58 Y. Saito, Rev. Polarogr., 1968, 15(6), 177-187.
- 59 P. Virtanen, R. Gommers, T. E. Oliphant, M. Haberland, T. Reddy, D. Cournapeau, E. Burovski, P. Peterson, W. Weckesser, J. Bright, S. J. van der Walt, M. Brett, J. Wilson,

- K. J. Millman, N. Mayorov, A. R. J. Nelson, E. Jones, R. Kern, E. Larson, C. J. Carey, İ. Polat, Y. Feng, E. W. Moore, J. VanderPlas, D. Laxalde, J. Perktold, R. Cimrman, I. Henriksen, E. A. Quintero, C. R. Harris, A. M. Archibald, A. H. Ribeiro, F. Pedregosa, P. van Mulbregt and SciPy 1.0 Contributors, *Nat. Methods*, 2020, 17, 261–272.
- 60 C. T. Campbell, ACS Catal., 2017, 7(4), 2770-2779.
- 61 J. Kestin, M. Sokolov and W. A. Wakeham, J. Phys. Chem. Ref. Data, 1978, 7, 941–948.
- 62 Z. Duan and S. Mao, Geochim. Cosmochim. Acta, 2006, 70(13), 3369–3386.
- 63 S. Sun, N. F. Dummer, T. Bere, A. J. Barnes, G. Shaw, M. Douthwaite, S. Pattisson, R. J. Lewis, N. Richards, D. J. Morgan and G. J. Hutchings, *Catal. Sci. Technol.*, 2022, 12, 3727–3736.
- 64 S. Wang, H. Li, M. He, X. Cui, L. Hua, H. Li, J. Xiao, L. Yu, N. P. Rajan, Z. Xie and D. Deng, *J. Energy Chem.*, 2019, 36, 47–50.
- 65 Z. Mao and C. T. Campbell, ACS Catal., 2019, 9(10), 9465–9473.